

Valley quantum interference in silicon

J. Salfi,¹ J. A. Mol,¹ R. Rahman,² G. Klimeck,² M. Y. Simmons,¹ L. C. L. Hollenberg,³ and S. Rogge^{1,*}

¹*Centre for Quantum Computation and Communication Technology, School of Physics,
The University of New South Wales, Sydney, NSW 2052, Australia.*

²*Purdue University, West Lafayette, IN 47906, USA.*

³*Centre for Quantum Computation and Communication Technology,
School of Physics, University of Melbourne, Parkville, VIC 3010, Australia.*

(Dated: March 20, 2014)

Electron and nuclear spins of donor ensembles in isotopically pure silicon experience a vacuum-like environment, giving them extraordinary coherence[1, 2]. However, in contrast to a real vacuum, electrons in silicon occupy quantum superpositions of valleys in momentum space. Addressable single-qubit and two-qubit operations in silicon require that qubits are placed near interfaces, modifying the valley degrees of freedom associated with these quantum superpositions and strongly influencing qubit relaxation and exchange processes[3, 4]. Yet to date, spectroscopic transport measurements only indirectly probe wavefunctions[5–8], preventing direct experimental access to valley population and donor position in devices. Here we directly probe the spatial substructure of electronic valley interference in single quantum states of individual subsurface donors, in real space and reciprocal space, employing scanning tunneling spectroscopy. The valley population is found to be within 5% of a bulk donor when ~ 3 nm from the interface indicating that valley perturbation-induced enhancement of spin relaxation will be negligible for depths > 3 nm. The observed valley interference will also render two-qubit exchange gates sensitive to atomic-scale variations in positions of subsurface donors[9, 10]. These results will also be of interest to emerging schemes proposing to encode information directly in valley polarization[11–16].

Fabrication of devices[17] and quantum control of spins in silicon[18, 19] has been accomplished at the single-donor level. However, addressable control and coupling within qubit arrays requires local gates and control interfaces, which strongly influence the electronic valley degrees of freedom[3–10, 20–24]. While these unconventional orbital degrees of freedom play no role in conventional silicon microelectronics, they invariably arise in quantized states in indirect gap materials, and are pervasive in quantum electronics. Atomic scale potentials of interfaces determine the valley physics of spin qubits in silicon[9, 10, 20, 21, 23] and graphene[22], emerging valley-based devices in silicon[12, 13] and valley pseudospin-based devices in graphene[11, 16].

The direct measurements of valley interference presented herein addresses spatial aspects of the 60-year old theory of shallow impurities in silicon[10, 21, 25, 26]. From direct comparison with theory, the z-valley population is estimated to be $\sim 38 \pm 2\%$ for a ~ 3 nm deep donor, perturbed by only $\sim 5\%$ compared with $\sim 33.3\%$ for a donor in bulk silicon. Consequently, donors more than 3 nm deep should not experience a significant valley-repopulation induced increase in spin-lattice relaxation. Moreover, the nearly bulk-like valley interference observed will render two-qubit exchange gates sensitive to atomic variations in donor position[9, 10], even for subsurface donors. This experimentally formed understanding of donor wavefunctions is essential for engineering spin qubit arrays leveraging silicon's exceptional coherence[1, 2].

We employed unconventional scanning tunneling spectroscopy (STS)-based spatially-resolved single-electron

transport to spatially measure valley interference in single quantum states of isolated subsurface arsenic donors. Ultra-high vacuum annealing, with parameters targeted to deplete the upper ~ 10 nm of donors[28], was performed on a highly arsenic-doped silicon wafer (see Methods). Spatially well-isolated residual As donors (density $\sim 10^{11} \text{ cm}^{-2}$) were found in the depletion region by subsurface imaging[29, 30] at $U = -1.25$ V.

The electronic isolation of donor-bound states within the depletion region was quantified as illustrated in Figure 1A, by single-electron transport spectroscopy employing the scanning tunneling microscope tip, at 4.2 K. The measured differential conductance dI/dU above donor 1 (Figure 1B, blue squares) exhibited the signature of single electron tunneling, as illustrated, from the substrate's impurity band[27], to the subsurface donor brought into the bias window by tip-induced band bending[29], to the tip. Fitting of the first two peaks to single-electron transport theory[31, 32](Figure 1B, red line) established a coupling $\hbar(\Gamma_{\text{in}} + \Gamma_{\text{out}}) \ll k_B T \sim 350 \mu\text{eV}$ for donor 1, similar to states in single dopant transistors[6]. The lowest energy peak ($U \approx -0.8$ V) was found to be bound to donor 1 in spatially resolved dI/dU (Figure 1C). Higher energy peaks ($U < -1.05$ V) in Figure 1B and 1C are two-electron states (see Supplementary Information).

Spatially resolved measurements of donor-bound states were carried out using an unconventional scheme. Constant current imaging of bound states[30, 33] was avoided since it necessarily measures multiple states. On the other hand, measurement of dI/dU vs. U on a two-dimensional spatial grid would be impractically time con-

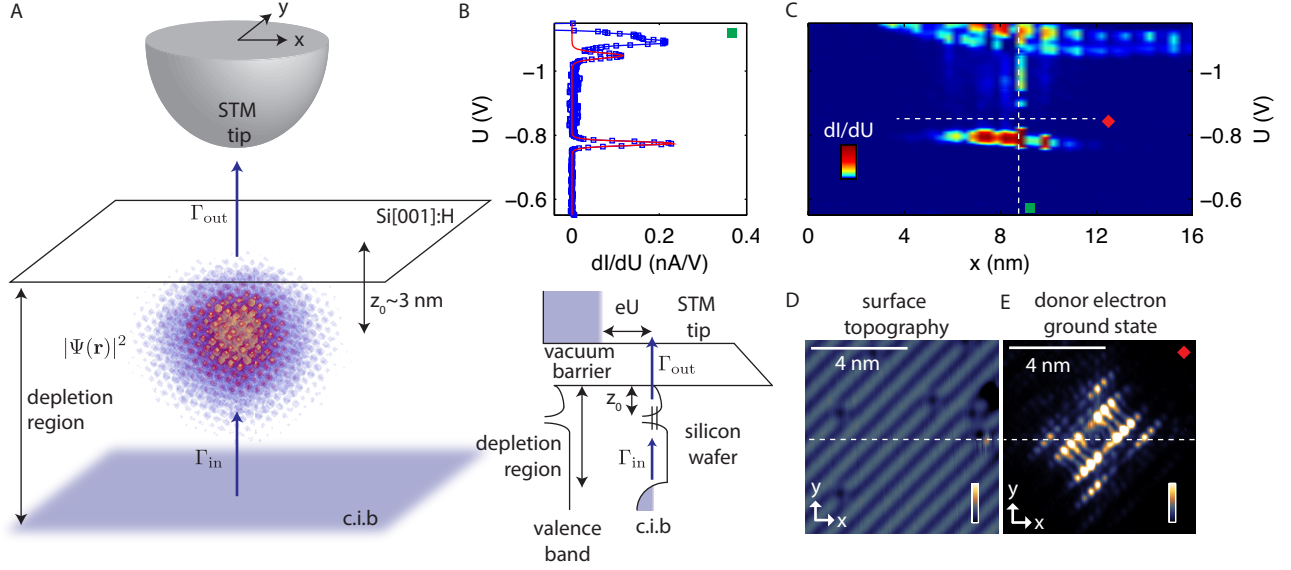


FIG. 1. **Spatial measurement of single quantum states of a subsurface donor** A. Illustration of single-electron tunneling from the conduction impurity band (c.i.b.) [27], to the subsurface donor in the depletion region with electron probability density $|\Psi(\mathbf{r})|^2$, to the tip. B. Top: Measured dI/dU (blue squares) for tip position above the subsurface donor, and least-squares fit to thermally broadened single-electron transport (red line). Bottom: Schematic band diagram, whereby the sample bias $U < 0$ brings the donor-bound states into resonance with the Fermi energy in the conduction impurity band (c.i.b.), which is spatially separated from the donor by a depletion region. C. Measured differential conductance dI/dU versus x and sample bias U , along line passing over single donor. Scale: (0,0.25) nA/V. Tip location for measurement in B is indicated by the vertical dashed line (green box). D. Constant current ($I_0 = 150$ pA) topography $z(x, y)$ recorded during first line scan at $U = -1.45$ V, a bias where there is minimal evidence of buried donor. Scale: (0,100) pm. E. Spatially resolved single-electron tunneling current $I(\mathbf{r}) \propto |\Psi(\mathbf{r})|^2$ through the single donor-bound state, for the same area as D, but with $U = -0.85$ V, and the feedback loop off. The signal vanishes away from the donor, as expected for a true single state measurement. White dashed line (red diamond) denotes where data in 1C was obtained. Scale: (0,0.35) nA.

suming for the spatial frequency range $|k_x|, |k_y| \geq 8\pi/a_0$ necessary to avoid frequency aliasing, and resolution $2\pi/50a_0$ necessary to resolve silicon's band structure. We therefore employed an unconventional two-pass line-scan to spatially measure individual donor-bound states. In the first pass of each line, the surface topography $z(x, y)$ was measured at $U = -1.45$ V. During the second pass of each line, a current $I(\mathbf{r})$ proportional to the probability density $|\Psi(\mathbf{r})|^2$ for a single bound state was measured, by choosing a bias ($U_2 = -0.85$ V for donor 1) that ensured a single state in the bias window for single-electron transport. The feedback loop was turned off as required for the second pass, and the tip position was set to $\mathbf{r} = (x, y, z(x, y) - \delta z)$, $\delta z = 0.25$ nm closer to the sample compared to the first line's topography. The value of δz was chosen such that $I(U_2) \sim \exp(\kappa z) \sim \Gamma_{\text{out}}$, or equivalently, $\Gamma_{\text{out}} \ll \Gamma_{\text{in}}$. In this regime, $I(\mathbf{r}) \propto |\Psi(\mathbf{r})|^2$, where \mathbf{r} is the central coordinate of the tip apex orbital [34]. For donor 1, the measured $z(x, y)$ and $I(\mathbf{r}) \propto |\Psi(\mathbf{r})|^2$ are shown in Figure 1D and Figure 1E, respectively. In Figure 1E, $|\Psi(\mathbf{r})|^2$ vanishes away from the donor, as expected for a true single state measurement.

To investigate valley interference of donor 1, we numerically computed the two-dimensional Fourier repre-

sentation of $I(\mathbf{r}) \propto |\Psi(\mathbf{r})|^2$, shown in Figure 2A. The vertices of the outer dashed box are reciprocal lattice vectors $2\pi/a_0(p, q)$ with $p = \pm 1$, $q = \pm 1$, and $a_0 = 0.54$ nm. Figure 2A contains the unmistakable signature of conduction band ellipsoids highlighted in green, along [100] (x) and [010] (y) directions. Positions of the conduction band minima of silicon [35] at $k_\mu = 0.85(2\pi/a_0)$ are indicated by white crosses. We term the structure outlined in blue within $k \lesssim 0.5(2\pi/a_0)$ the probability envelope, because it contains the lowest spatial frequencies of the probability density. Dashed outlined features centered at $2\pi/a_0(\pm 1/2, \mp 1/2)$ and $2\pi/a_0(\pm 1/2, \pm 1/2)$ are created by the 2×1 reconstruction, and are related to the probability envelope and ellipsoids, respectively, as evidenced by their $2\pi/a_0(\mp 1/2, \pm 1/2)$ displacement (white arrows, Figure 2A) relative to them. The depth of donor 1 was estimated to be $z_0 = (5 \pm 1)a_0$ nm (20 ± 4 lattice planes), as described in Methods. Shown for comparison in Figure 2B is the Fourier transform of the vacuum tail of the ground state probability density $|\Psi_1(\mathbf{r})|^2$ obtained by empirical $\text{sp}^3\text{d}^5\text{s}^*$ tight-binding (see Methods).

The shape and position of the predicted ellipsoids (green) and probability envelope (blue) in Figure 2B are in very good agreement with measurements in Fig-

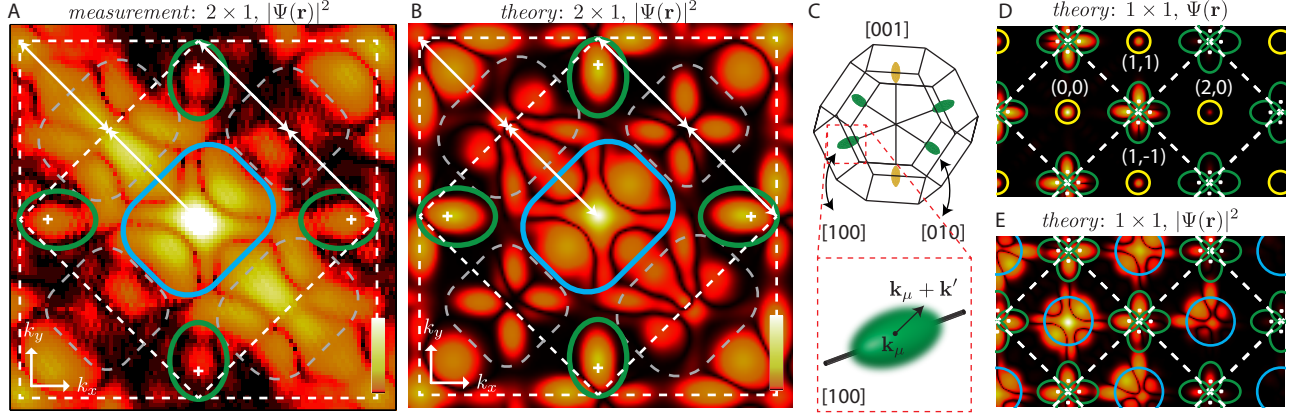


FIG. 2. **Valley interference of a single quantum state in reciprocal space: measurement and theory** A. Fourier amplitude of measured $I(\mathbf{r}) \propto |\Psi(\mathbf{r})|^2$ for donor-bound electron in Figure 1. Corners of outer dashed square are reciprocal lattice vectors $2\pi/a_0(p, q)$ with $p = \pm 1$ and $q = \pm 1$. White crosses denote $k_\mu = 0.85(2\pi/a_0)(\pm 1, 0)$ and $k_\mu = 0.85(2\pi/a_0)(0, \pm 1)$. Ellipsoids structures are found within green boundaries, probability envelope is found within blue boundaries, and 2×1 reconstruction-induced features are found within grey dashed boundaries. B. Calculated Fourier amplitude of single-electron (D^0) ground state probability density $|\Psi(\mathbf{r})|^2$ for $z_0 = 6.25a_0 \approx 3.4$ nm deep donor, with a 2×1 surface reconstruction. C. Distribution of momenta about valley minima in the $x - y$ (surface) plane (green ellipsoids) and perpendicular to it (yellow ellipsoids), and close up of single valley distribution $F_x(\mathbf{k}')$. D. Overlay of reciprocal space model for D^0 ground state wavefunction on atomistic calculation of $\Psi(\mathbf{k})$ using tight-binding method. Labeled wave vectors are in units: $2\pi/a_0$. E. Overlay of reciprocal space model for the D^0 ground state probability density on atomistic calculation using tight-binding method. For D and E, a 1×1 reconstruction was assumed for simplicity.

ure 2A. Both of the ellipsoids and probability envelope originate from electronic quantum interference among the six valleys of silicon's conduction band (Figure 2C, top), whose coherent population is described by valley quantum numbers α_μ ($\mu = 1 \dots 6$). The α_μ are multiplicative prefactors in the reciprocal space distribution $F_\mu(\mathbf{k}')$ (Figure 2C, bottom) of the wavefunction over the Bloch functions $\phi_{\mathbf{k}_\mu + \mathbf{k}'}(\mathbf{r})$ belonging to different minima \mathbf{k}_μ . The i^{th} donor-bound eigenstate can be written as $\Psi_i(\mathbf{r}) = \sum_\mu \alpha_\mu^i \int d\mathbf{k}'^3 F_\mu(\mathbf{k}') \phi_{\mathbf{k}_\mu + \mathbf{k}'}(\mathbf{r})$ (see reference 10). For a donor in bulk silicon, the ground state is a spin degenerate valley singlet with $\alpha^1 = 6^{-1/2}[1, 1, 1, 1, 1, 1]$. For arsenic, the singlet ionization energy is 52 meV, 22 meV below the spin-degenerate excited valley triplet with $\alpha^2 = 2^{-1/2}[1, -1, 0, 0, 0, 0]$, $\alpha^3 = 2^{-1/2}[0, 0, 1, -1, 0, 0]$, and $\alpha^4 = 2^{-1/2}[0, 0, 0, 0, 1, -1]$. The constructive valley interference of the singlet at the arsenic site (the central cell) is responsible for the energy difference[25, 26].

The coherent population of valleys represented by α^i determines the Fourier decomposition of both $\Psi(\mathbf{r})$ and $|\Psi(\mathbf{r})|^2$, as follows. Writing $\phi_{\mathbf{k}}(\mathbf{r}) = \exp(i\mathbf{k} \cdot \mathbf{r})u_{\mathbf{k}}(\mathbf{r})$ and $u_{\mathbf{k}}(\mathbf{r}) = \sum_{\mathbf{G}} A_{\mathbf{k}, \mathbf{G}} \exp(i\mathbf{G} \cdot \mathbf{r})$, where $\mathbf{G} = [p, q, r] = [0, 0, 0], [1, 1, 1], [2, 0, 0], [2, 2, 0], [3, 1, 1], \dots$ (units: $2\pi/a_0$) and their equivalents are the reciprocal lattice vectors with nonzero $A_{\mathbf{k}, \mathbf{G}}$ in silicon[36], we obtain[10]

$$\Psi_i(\mathbf{r}) = \sum_{\mathbf{G}} \sum_{\mu} \int d\mathbf{k}'^3 \alpha_\mu^i A_{\mathbf{k}_\mu + \mathbf{k}', \mathbf{G}} F_\mu(\mathbf{k}') e^{i(\mathbf{G} + \mathbf{k}_\mu + \mathbf{k}') \cdot \mathbf{r}}. \quad (1)$$

This expression directly gives the Fourier component

$\Psi^i(\mathbf{k}) = \alpha_\mu^i A_{\mathbf{k} - \mathbf{G}, \mathbf{G}} F_\mu(\mathbf{k}')$ for $\mathbf{k} = \mathbf{G} + \mathbf{k}_\mu + \mathbf{k}'$, and can be seen as a valley distribution (inner sum/integral) repeated with a different prefactor $\alpha_\mu^i A_{\mathbf{k} - \mathbf{G}, \mathbf{G}}$ for each reciprocal lattice vector \mathbf{G} (outer sum), which appears at $\mathbf{G}_2 = [p, q]$ in our two-dimensional measurements. Green ellipsoids in Figure 2D centered at $\mathbf{G}_2 \pm \hat{x}k_\mu$ ($\mathbf{G}_2 \pm \hat{y}k_\mu$) are present when $\alpha_{\pm x}^i \neq 0$ ($\alpha_{\pm y}^i \neq 0$), while the yellow circle at \mathbf{G}_2 is a projected ellipsoid, present when $\alpha_{\pm z}^i \neq 0$. Atomistic calculations are also presented in Figure 2D for a 3.4 nm deep donor.

For a particular α_i there is a corresponding valley interference pattern in the orbital probability density $|\Psi_i(\mathbf{r})|^2 = \Psi_i^*(\mathbf{r})\Psi_i(\mathbf{r})$, determined by the following mapping. A Fourier component $\exp(-i\mathbf{k}' \cdot \mathbf{r})$ in $\Psi_i^*(\mathbf{r})$ and $\exp(i\mathbf{k}'' \cdot \mathbf{r})$ in $\Psi_i(\mathbf{r})$ map to $\exp(i(\mathbf{k}'' - \mathbf{k}') \cdot \mathbf{r})$ in $\Psi_i^*(\mathbf{r})\Psi_i(\mathbf{r})$. Using this mapping, ellipsoids at $\mathbf{k} \approx \mathbf{G}_2 \pm \hat{x}k_\mu$ ($\mathbf{k} \approx \mathbf{G}_2 \pm \hat{y}k_\mu$) in $|\Psi_i(\mathbf{r})|^2$, overlaying atomistic calculations in Figure 2E, arise from off-diagonal product terms of z valleys at $\mathbf{k}' \approx \mathbf{G}_2'$ and x (y) valleys at $\mathbf{k}'' \approx \mathbf{G}_2'' \pm \hat{x}k_\mu$ ($\mathbf{k}'' \approx \mathbf{G}_2'' \pm \hat{y}k_\mu$). Consequently, the ellipsoids in the Fourier decomposition of $|\Psi(\mathbf{r})|^2$ are direct evidence for the presence of all three valleys in the measured (Figure 2A) and atomistically calculated (Figure 2B) subsurface donor ground state. From the same mapping, the probability envelope (blue outline in Figure 2E) is obtained from $-\mathbf{k}'$ and \mathbf{k}'' in $\Psi_i^*(\mathbf{r})$ and $\Psi_i(\mathbf{r})$ both chosen either from the set $\{\mathbf{G}_2 \pm \hat{x}k_\mu, \mathbf{G}_2 \pm \hat{y}k_\mu\}$ of x and y valley terms, or the set $\{\mathbf{G}_2\}$ of projected z valleys terms. It follows from the mapping that x , y , and z valleys con-

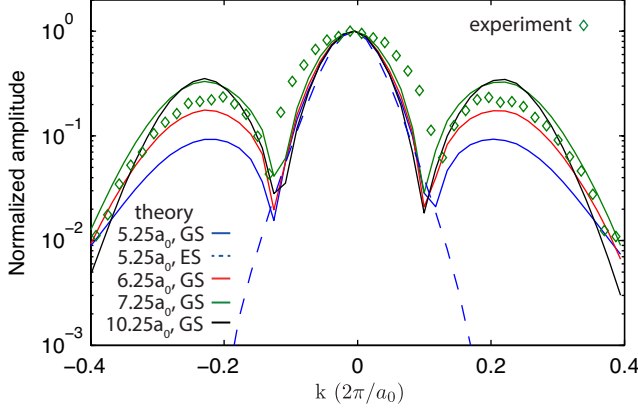


FIG. 3. **Valley population** Comparison of measured (green diamonds) and theoretical (solid lines) reciprocal space profile of $|\Psi_1(\mathbf{r})|^2$ for donor ground state, along 110 direction in reciprocal space. The height of the central peak ($k = 0$) relative to side peaks ($k = 0.15(2\pi/a_0)(\pm 1, \pm 1)$) increases with decreasing depth from $10.25a_0$ (black line), $7.25a_0$ (green line), $6.25a_0$ (red line), to $5.25a_0$ (blue line), indicating repopulation from x and y valleys into z valleys with decreasing depth. The calculated first excited state, shown for $5.25a_0$ (blue dashed line), populates only the z valley, and hence, has no side lobes.

tribute to the peak at $k = 0$, while only x and y valleys contribute to the side peak at $k = 0.15(2\pi/a_0)(\pm 1, \pm 1)$.

We compare the relative heights of the central and side peaks in the measured and calculated ground state probability envelopes to quantify the deviation from a bulk-like valley configuration for donor 1. Calculations presented in Figure 3 demonstrate an increasing relative contribution of the central peak indicating a relative increase in the population of z -valleys relative to x and y , with decreasing depth $10.25a_0$ to $5.25a_0$, in zero electric field. This arises from the competition between the interface, which introduces a valley-orbit potential and also tends to depopulate the x and y valleys with lighter masses parallel to the interface, and the donor ion's valley-orbit potential, which prefers to keep them equal. The side peak amplitude saturates at a depth $7.25a_0$ indicating that the valley configuration approaches that of a donor in bulk silicon. Shown in Figure 3, the measured donor (green diamonds)'s profile agrees with calculations for donors of $7.25a_0$ and $6.25a_0$ depths, which have z -valley populations of 36% and 40%, respectively (See Supplementary Information). Therefore, we estimate that the z -valley configuration of the measured donor differs by only $\sim 5\%$ compared to a donor in bulk silicon (33.3%). The discrepancy compared to the extracted depth $(5 \pm 1)a_0$ is at the level of a single lattice constant, and could arise from electric fields present in the experiment that are not accounted for in the theory. Moreover, the wider central peak in measurements could be the result of slightly enhanced lateral localization due to image charges associ-

ated with dielectric mismatch for the 3 nm deep donor, also not taken into account in the theory. Overall, the agreement of the reciprocal space profile with the theoretical description from the calculations is remarkable. Note that low-pass response of the STM tip orbital is not expected for such low spatial frequencies $k \lesssim 0.21(2\pi/a_0)$ ($\lambda \gtrsim 2.6$ nm).

The real-space representation of the ellipsoids, shown in Figure 4A and obtained by digital Fourier filtering, resemble a low frequency s-like envelope modulated by x and y -directed standing wave patterns with wavelength $\lambda_\mu \approx 2\pi/k_\mu = 0.65$ nm. As described above, the ellipsoids in $|\Psi_1(\mathbf{r})|^2$ arise from cross terms between the x (y) valleys, which oscillate at $\mathbf{k} = k_\mu \hat{x}$ ($\mathbf{k} = k_\mu \hat{y}$), and the z valley. Consequently, their real-space representation can be easily shown (see Supplementary Information) to have the form $F_z(\mathbf{r})(F_x(\mathbf{r})\cos(k_\mu x) + F_y(\mathbf{r})\cos(k_\mu y))$, where $F_i(\mathbf{r}) = \int d^3\mathbf{k}' F_i(\mathbf{k}') \exp(i\mathbf{k}' \cdot \mathbf{r})$ is the donor ground state envelope function. The maximum of the real-space oscillation pattern, labelled with a red cross in Figure 4, identifies the position of the ion. Notably, the appearance of elongation along $[100]$ and $[010]$ directions (Figure 4A) is also predicted by atomistic theory (Figure 4B).

Like the ellipsoids, the probability envelope arises from valley interference. Therefore, it is not surprising that the real-space representation of the probability envelope in Figure 4C has an unusual shape characterized by a node along $x = -y$. This node, predicted by calculations (Figure 4D), contrasts the simple envelope of oscillations in Figure 4A/4B. Notably, a survey of over thirty sub-surface donors with indistinguishable spectral signatures revealed two distinct ground state probability envelopes: type-A of which donor 1 in Figure 4C is a typical example, and type-B, of which donor 2 in Figure 4E is a typical example. While the ellipsoid interference pattern of the type-B donor (Figure 4E) resembles that of type-A donor (Figure 4A), the probability envelope of the type-B donor (Figure 4G) has a protrusion along $x = -y$.

The type-A and type-B probability envelopes are at first peculiar. An examination of tight-binding calculations of $|\Psi(\mathbf{r})|^2$ for donors occupying successively deeper planes revealed a sequence A, A, B, B, A, A, B, B for donor depths $5.00a_0$, $5.25a_0$, $5.50a_0$, $5.75a_0$, $6.00a_0$, $6.25a_0$, $6.50a_0$, and $6.75a_0$. For the type-B donor, both the calculated ellipsoids (Figure 4F) and probability envelope (Figure 4H) are in excellent agreement with measurements in Figure 4E and Figure 4G, respectively. Moreover, the calculated probability envelope for a fixed donor depth was found to depend sensitively on the lattice plane below the surface where it was evaluated. The two different probability envelopes are therefore a manifestation of (1) rapid spatial variation of $|\Psi(\mathbf{r})|^2$ along z with lattice and valley spatial frequencies (and their harmonics), and (2) the relative sensitivity of the tip to the topmost atomic planes. Nevertheless, the spatial average of type-A and type-B probability envelopes is s-like, as

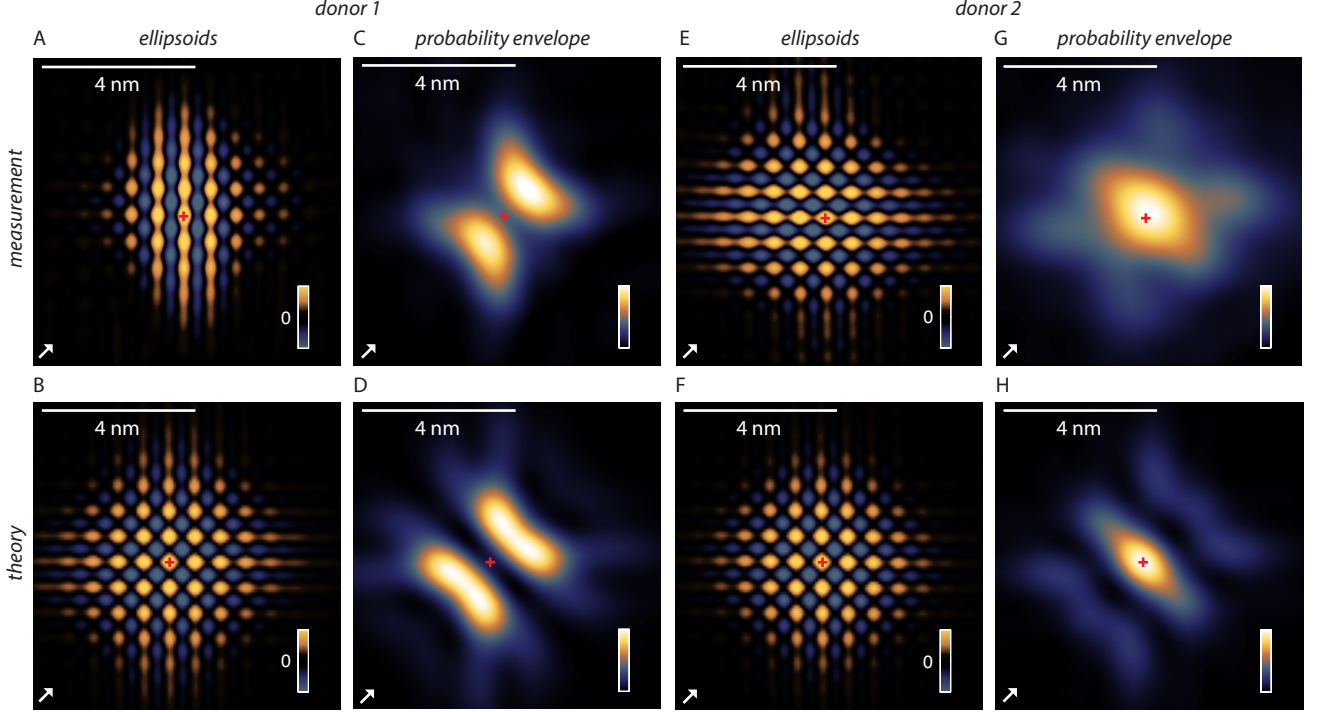


FIG. 4. **Valley interference of a single quantum state in real space: measurement and atomistic theory** A. Measured real-space representation of four ellipsoid features at $k \approx k_\mu$ for donor 1 in Figure 2, obtained by frequency selective inverse Fourier transform of Figure 2A. Scale: (-15,15) pA. Arrow denotes [110] dimer direction. Red cross denotes ion position determined from real-space ellipsoid pattern, as discussed in Supplementary Information. B. Predicted real-space representation of four ellipsoid features based on atomistic calculations. The best match was obtained for $z_0 = 6.25a_0 \approx 3.4$ nm deep donor. C. Measured real-space representation of probability envelope. D. Predicted real-space representation of type-A probability envelope. E. Same as A, but for measured donor 2 with type-B probability envelope. F. Predicted real-space representation of four ellipsoid features based on atomistic calculations. The best match was obtained for a $z_0 = 6.75a_0 \approx 3.7$ nm deep donor. G. Same as B, but for type-B probability envelope. H. Predicted real-space representation of probability envelope based on atomistic calculation for F.

expected from effective mass[25].

Any interface-induced mixing with excited valley-orbit states enhances the spin-lattice relaxation rate[37]. The nearly bulk-like valley interference pattern observed for ~ 3 nm deep donors is a direct indication of small mixing with valley-orbit excited states, such that for > 3 nm deep arsenic donors, the spin-lattice relaxation rate T_1^{-1} is not enhanced compared with bulk donors. For magnetic fields of practical interest[38], T_1 of subsurface donors will still greatly exceed the spin coherence time of electrons in isotope purified silicon[1]. However, proximity to non-ideal interfaces could introduce other relaxation processes. Moreover, the observed interference in Figure 4 is precisely the phenomena predicted to render two-qubit gates sensitive to atomic-scale variations in donor position[9, 10]. This can be thought of as a direct consequence of phase mismatch in interfering terms in the exchange interaction $J(\mathbf{R}) = \int \Psi^*(\mathbf{r}_1 - \mathbf{R})\Psi^*(\mathbf{r}_2)V_{ee}(|\mathbf{r}_1 - \mathbf{r}_2|)\Psi(\mathbf{r}_1)\Psi(\mathbf{r}_2 - \mathbf{R})$ between donors separated by a displacement \mathbf{R} , each having lattice-incommensurate ($\lambda = 0.65$ nm) spatial oscillations.

lations.

The spatially resolved single electron transport demonstrated herein provides a new level of access to valley physics not available in single-electron transport spectroscopy of donors in nanoscale transistors[6, 7, 17]. The quantification of interface-induced valley repopulation is accompanied by direct and accurate determination of donor depth, and observation of the interface and crystal environment of the dopant. Most importantly, the coherent electronic valley interference and population of the donor atom is found to be remarkably robust to the presence of nearby (~ 3 nm away) interface perturbations. This new level of understanding is essential to the engineering of addressable single-qubit two-qubit operations in silicon devices[9, 10, 20, 21, 39], in order to exploit silicon's remarkable coherence[1, 2].

The authors would like to thank J. Verduijn for helpful discussions. This work is supported by the European Commission Future and Emerging Technologies Proactive Project MULTI (317707) and the ARC Centre of Excellence for Quantum Computation and

Communication Technology (CE110001027). This work is part of the research program of the Foundation for Fundamental Research on Matter (FOM), which is part of the Netherlands Organization for Scientific Research (NWO). S.R. acknowledges a Future Fellowship (FT100100589). M.Y.S acknowledges a Federation Fellowship. This research was also supported in part by the U.S. Army Research Office (W911NF-08-1-0527).

APPENDIX A: METHODS

Sample preparation

Samples where single-electron tunneling through donor-bound electronic states was observed were prepared by flash annealing a commercial n-type (arsenic doped) silicon wafer with resistivity $0.004 - 0.001$ ohm-cm to a temperature ~ 1050 °C for 10 seconds, a total of 3 times. After the final flash anneal, the temperature was rapidly quenched to 800 C, followed by slow (1 °C/s) cooling to 340 °C, producing a 2×1 surface reconstruction. Hydrogen passivation was carried by dosing with 9 monolayers of atomic hydrogen. This flash anneal procedure is known from secondary ion mass spectroscopy to deplete the upper ~ 10 nm of the wafer of arsenic dopants[28], but is shallow enough to maintain sufficient coupling to the conduction impurity band to obtain a measurable single-electron tunneling current through donor-bound states. No donors were found for samples flashed 3 times at 1200 °C, which are expected to have too deep (~ 100 nm) a surface depletion and too few residual arsenic dopants[28].

Measurement

Measurements were performed using an Omicron low temperature scanning tunneling microscope (LT-STM) operating in ultra-high vacuum at a temperature of 4.2 K. Current I was measured as a function of sample voltage U using ultra-low noise electronics, and dI/dU was obtained by numerical differentiation. Spatially resolved measurements of donors were obtained on frames 20 nm \times 20 nm in size, containing a single subsurface dopant, with a spatial resolution of $0.02 - 0.04$ nm. Fine calibration of reciprocal lattice vector positions was carried out by Fourier transforming topographies (see Supplementary Information) acquired simultaneously with quantum states, using the multi-line scan technique.

The depth z_0 of donor 1 was estimated by fitting the spatial variation $\Delta E_C(x, y)$ of the conduction band edge to a dielectric-screened Coulomb potential including the

vacuum-dielectric mismatch,

$$\Delta E_C(x, y) = \frac{-e^2}{4\pi\epsilon_0\epsilon_{\text{eff}}} \frac{1}{\sqrt{x^2 + y^2 + z_0^2}}. \quad (2)$$

Here, x and y describe the lateral position of the tip, $\epsilon_{\text{eff}} = (1 + \epsilon_2)/2$, and ϵ_2 is the dielectric constant of silicon. The conduction band is probed for $U > 0$, a condition where tip-induced band bending ionizes the donor and depletes the surface of carriers, justifying the fit to an unscreened Coulomb potential, as described in detail elsewhere[32]. For the donor 1 in Figure 1 we found $z_0 = 2.8 \pm 0.45 \approx (5 \pm 1)a_0$ nm and $\epsilon_{\text{eff}} = 6.1 \pm 1$, closely matching the expected value $\epsilon_{\text{eff}} = (1 + 11.7)/2 = 6.35$ for a Coulomb potential a depth z_0 below the silicon/vacuum interface.

APPENDIX B: SUPPLEMENTARY INFORMATION

Conventional subsurface dopant imaging

Conventional subsurface dopant imaging[29, 30] at a constant current and bias $U = -1.25$ V was initially used to identify subsurface donors, as discussed in the main text. The signature of bound states in the measured topography is the localized protrusion seen in Figure 6.

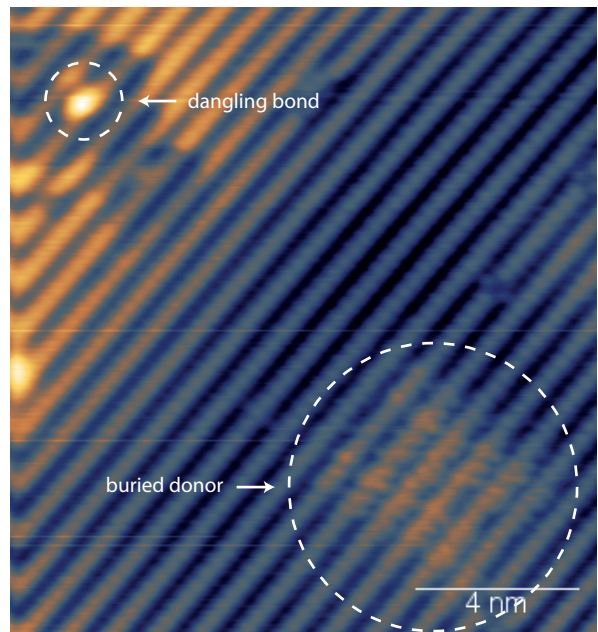


FIG. 5. Signature of subsurface donor found at sample bias $U = -1.25$ V.

As apparent from Figure 1B in the main text, localized states at $U = -0.80$ V, $U = 1.05$ V and $U = -1.09$ V all contribute to the constant current image obtained at

donor	donor 1	donor 2
U_1 (V)	0.7742 ± 0.0002	0.7567 ± 0.00051
U_2 (V)	1.0488 ± 0.0005	1.0241 ± 0.00043
α_1	0.0878 ± 0.0033	0.0632 ± 0.0110
α_2	0.0627 ± 0.0049	0.0813 ± 0.0110
$\hbar\Gamma_1/k_B T$	-	5.1264 ± 1.0433
$\hbar\Gamma_2/k_B T$	-	2.8345 ± 0.6472
$\frac{1}{2}\hbar\Gamma_1/3.5k_B T$	-	0.7323 ± 0.1490
$\frac{1}{2}\hbar\Gamma_2/3.5k_B T$	-	0.4049 ± 0.0925
$E_2 - E_1$ (meV)	21 ± 2	20 ± 3

TABLE I. Results for least-squares fits of data in Figure 6 and 7 to model discussed in methods. Donor 1 was fit to purely thermally broadened resonances.

$U = -1.25$ V. In general, the local density of states of the band edge into which tunneling also necessarily occurs in constant current imaging will be modified by neutral impurity scattering[29]. The combination of tunneling from multiple bound states and a continuum disturbed near the donor by neutral impurity scattering, makes constant current imaging unsuitable for probing single quantum states of subsurface donors. Interestingly, the topography taken at a sample bias $U = -1.45$ V (Figure 1D, main text) shows no evidence for the subsurface donor. Donors discussed in the main text were identified using the two-pass line-scan.

Single-electron transport spectroscopy

In this section, the single-electron tunneling spectra measured for tip positions above donors 1 and 2 are discussed within the theory of single-electron transport in the weak coupling regime[31], which describes similar experiments on p-type dopants in silicon[32], and transport experiments on single-atom transistors[?].

The single-electron transport tunneling current measured for a tip position above donor 1 (Figure 1 and 2) in the main text is presented for several tip heights in Figure 6A. Sequentially from the top to bottom, data correspond to 8 different tip heights each successively 28 pm higher above the dopant. Blue data points are for the tip height presented in Figure 1B in the main text. The nearly fixed offset (on a logarithmic scale) between curves obtained at different tip heights reflects the exponential suppression of the wavefunction, which can only be observed when $\Gamma_{out} \ll \Gamma_{in}$ (Figure 1B) in a single-electron tunneling experiment in the STM. From $\Gamma_{out} \ll \Gamma_{in}$ we have $I(\mathbf{r}) \propto |\Psi(\mathbf{r})|^2$.

On a logarithmic scale, the linear drop of current into the noise floor (~ 50 fA) is the clear experimental signature of thermal broadened single-electron transport[31]. State energies $E_i = e\alpha U_i$ were obtained by least-squares

fitting of the lever arm α and voltage U_i to the well-known line shape for single-electron tunneling[31], as recently employed to describe similar experiments on p-type dopants in silicon[32]. The measured current $I(U)$ was fit to $I = \int_0^U (\partial I(U')/\partial U') dU'$, where

$$\frac{\partial I}{\partial U} = \sum_i A_i \int_{-\infty}^{\infty} dE \frac{\frac{1}{2}\hbar\Gamma_i \times \cosh^{-2}(E/2k_B T)}{(\frac{1}{2}\hbar\Gamma_i)^2 + (\alpha e(U - U_i) - E)^2}, \quad (3)$$

and Γ_i and A_i are lifetimes and amplitudes for states $i = 1, 2$. The proportionality constant A_i was allowed to vary linearly with tip height to account for a small positive differential conductance that arises either by (a) field-induced lowering of the barrier to the STP tip, or (b) an increase in the tunneling density of states in the tungsten tip, which both could occur with increasing bias U . Results for the fit of donor 1 are given in Table I, along with the energy splitting $E_2 - E_1 = \frac{1}{2}e(\alpha_1 + \alpha_2)(U_2 - U_1)$ estimated assuming a linear variation of α with voltage.

Figure 6B shows the least-square fits of the measured current I (black squares) to the model discussed above (red line), as well as numerically differentiated conductance dI/dU (blue circles), and the derivative of the least square fit (green line). The same results plotted on a linear scale are presented in Figure 6C.

The single-electron tunnel current spectrum of donor 2 from the main text is presented for several tip heights in Figure 7A. Data (green squares) are shown for 13 tip heights each successively 14 pm higher above the dopant. The upturn in the logarithm of the tunnel current indicates that the single-electron transport is not purely thermally broadened[31]. However, the broadening of each step does not change with increasing current, ruling out broadening by dynamical charge fluctuations, as discussed elsewhere[32]. Rather, the upturn reflects a measurable contribution from lifetime broadening associated with the coupling of the donor electron to the conduction impurity band. This could occur in donor 2 and not in donor 1, for example, due to local differences in the depth of the flash annealing-induced local depletion, of either a purely statistical nature, or due to a temperature gradient in the sample during annealing.

The curve plotted in blue circles in Figure 7A was fit to a model of thermally broadened Lorentzians (red line) in the sample voltage range -0.65 V to -1.08 V. Figure 7B shows the least-square fits of the measured current I (black squares) to the model (red line), as well as numerically differentiated conductance dI/dU (blue circles), and the derivative of the least square fit (green line). The same results plotted on a linear scale are presented in Figure 7C. Results for the fit of donor 2 are given in Table I.

Two additional dI/dU peaks were consistently found at a sample bias $U \sim -1.0$ V to $U \sim -1.1$ V, exemplified by those in Figure 1B/1C in the main text. These states consistently merged into tip-induced states for tip posi-

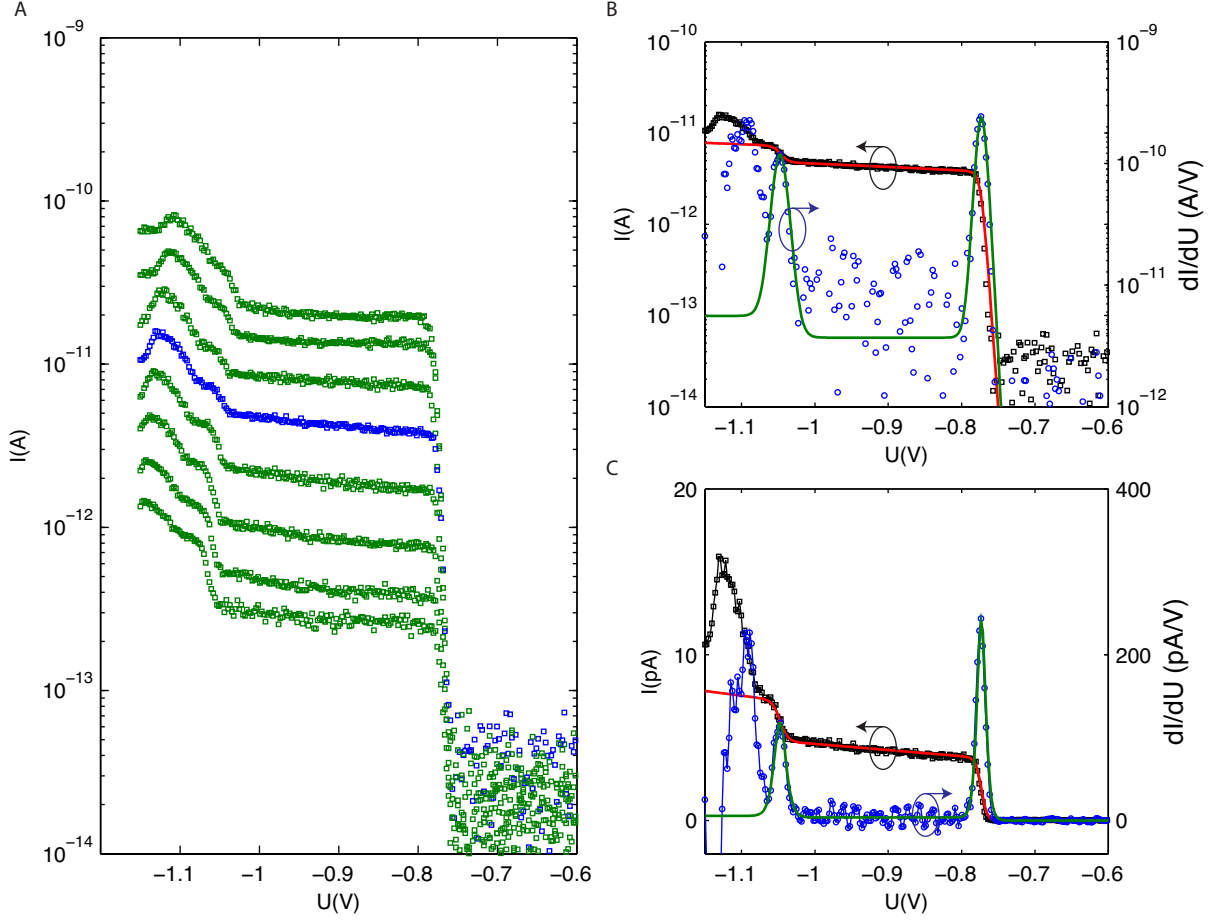


FIG. 6. A. Measured single electron tunneling current for different tip heights above donor 1 in the main text. B. Measured current I (black squares), numerical derivative dI/dU (blue circles), least-square fit to current (red line), and corresponding derivative of fit (green line). C. Same as B but plotted on a linear scale.

tions away from the donor (see Figure 1C, main text), and can therefore directly be identified as two-electron states for tip positions above the donor. Indeed, since $\Gamma_{\text{out}} \ll \Gamma_{\text{in}}$ in our experiment, single-electron excited states are only observed if they have both (1) different couplings Γ_{out} to the tip and (2) lifetime exceeding the rate Γ_{out} . Excited states in this situation may therefore be faint or not necessarily observed[?].

The energy difference between the states, 21 ± 2 meV for donor 1 and 20 ± 3 meV for donor 2, (obtained by least-squares fitting in Table I) is therefore the subsurface donor charging energy, much less than the ~ 50 meV value of arsenic in bulk silicon. These results are consistent with suppressed charging energies of subsurface arsenic donors observed in FinFETs, resulting from a dielectric-mismatch induced enhancement of the two-electron binding energy[?]. The spatial structure of these transitions, theoretically represented by an overlap between the one-electron and two-electron states[?], has both probability envelope and ellipsoid features in recip-

rocal space. However, an analysis of these features is well beyond the scope of the present work.

While the state at voltage $U_2 = -1.051$ V is therefore the two-electron singlet, the state at $U_3 = -1.094$ V is a two-electron triplet likely to involve an excited orbital with a different valley configuration. The absolute energy difference $E_3 - E_2 = e\alpha(U_3 - U_2)$ can be estimated using the value of $\alpha = 0.065 \pm 0.005$ extracted for peak 2. We obtain $E_3 - E_2 = 2.8 \pm 0.2$ meV, slightly higher than for donors near a silicon-SiO₂ interface in a nanoscale transistor[?].

Reciprocal lattice vectors and reconstruction-induced features

In this section we discuss calibration of reciprocal lattice vector positions, carried out using Fourier transforms of measured topographies, as well as the appearance and origin of reconstruction-induced features in both the to-

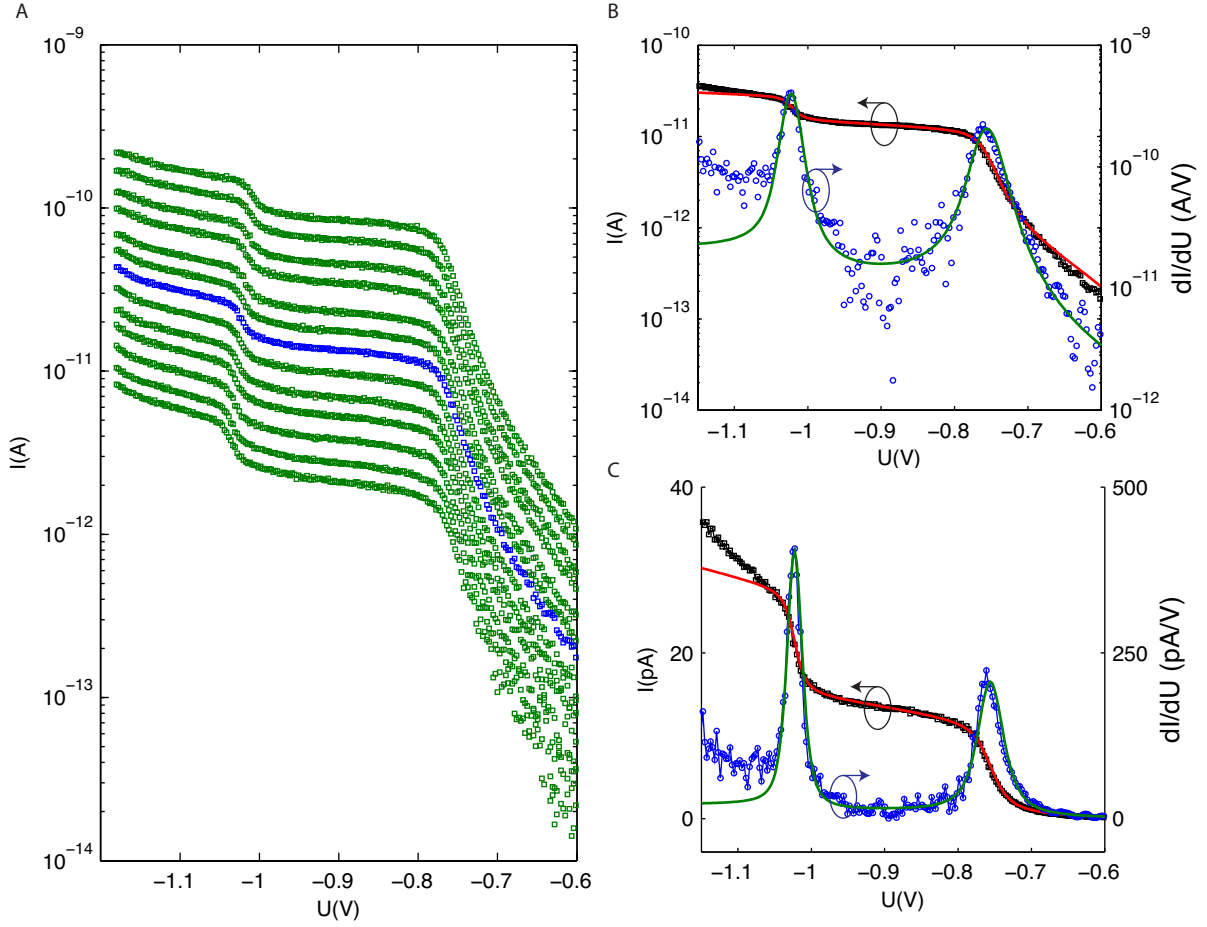


FIG. 7. A. Measured single electron tunneling current for different tip heights above donor 2 in the main text. B. Measured current I (black squares), numerical derivative dI/dU (blue circles), least-square fit to current (red line), and corresponding derivative of fit (green line). C. Same as B but plotted on a linear scale.

pographies and measured quantum states, and the associated sampling requirements to faithfully represent them in the measurements.

The topography $z(x, y)$ measured simultaneously with donor 1 (donor 2) in the main text is given in Figure 8A (8D). Peaks at reciprocal lattice frequencies in the the corresponding Fourier transform for donor 1 (donor 2) given in Figure 8B (8E) were employed to carry out a fine calibration of the coordinate system. Results are shown after calibration correcting a trivial rotational misalignment of the cleaved $10 \text{ mm} \times 3$ sample within the sample plate, and a small tip drift[?] ($< 0.1 \text{ nm/hour}$) of the 4.2 K LT-STM during the ~ 30 minute measurement of each donor.

The result is the alignment of reciprocal lattice vector positions $2\pi/a_0(\pm 1, \pm 1)$ in the measured topography with spots corresponding to the cubic lattice constant $a_0 = 0.54 \text{ nm}$ of the silicon surface. Peaks at $2\pi/a_0(\pm 1/2, \mp 1/2)$ originate from the 2×1 surface reconstruction. The latter, created by symmetric dimerization

of the hydrogen terminated silicon surface[43], are found at a displacement $\Delta \mathbf{G} = 2\pi/a_0(\mp 1/2, \pm 1/2)$ relative to reciprocal lattice vectors positions. Features centered at the same coordinates were observed in the Fourier transform of the orbital probability density of donor 1 (Figure 2A and Figure 8C) and donor 2 (Figure 8F), a displacement of $\Delta \mathbf{G}$ from probability envelope features at $\mathbf{k} = 2\pi/a_0(\pm 1, \pm 1)$ and $k = 0$. Similarly, the structure found at $2\pi/a_0(\pm 1/2, \pm 1/2)$ for donor 1 (Figure 8C) and donor 2 (Figure 8F) is related to the four symmetric ellipsoids centered around $2\pi/a_0(0, \pm 1)$ and $2\pi/a_0(\pm 1, 0)$, as evidenced by the $\Delta \mathbf{G} = 2\pi/a_0(\mp 1/2, \pm 1/2)$ displacement relative to these structures.

For the sake of simplicity, the first Brillouin zone of measured and calculated Fourier representations is shown. However, measurements reveal nonzero components with spatial frequencies to at least $2(2\pi/a_0)$. The Nyquist sampling theorem therefore dictates a minimum spatial sample frequency exceeding $4(2\pi/a_0)$. Using our single quantum state imaging method we could

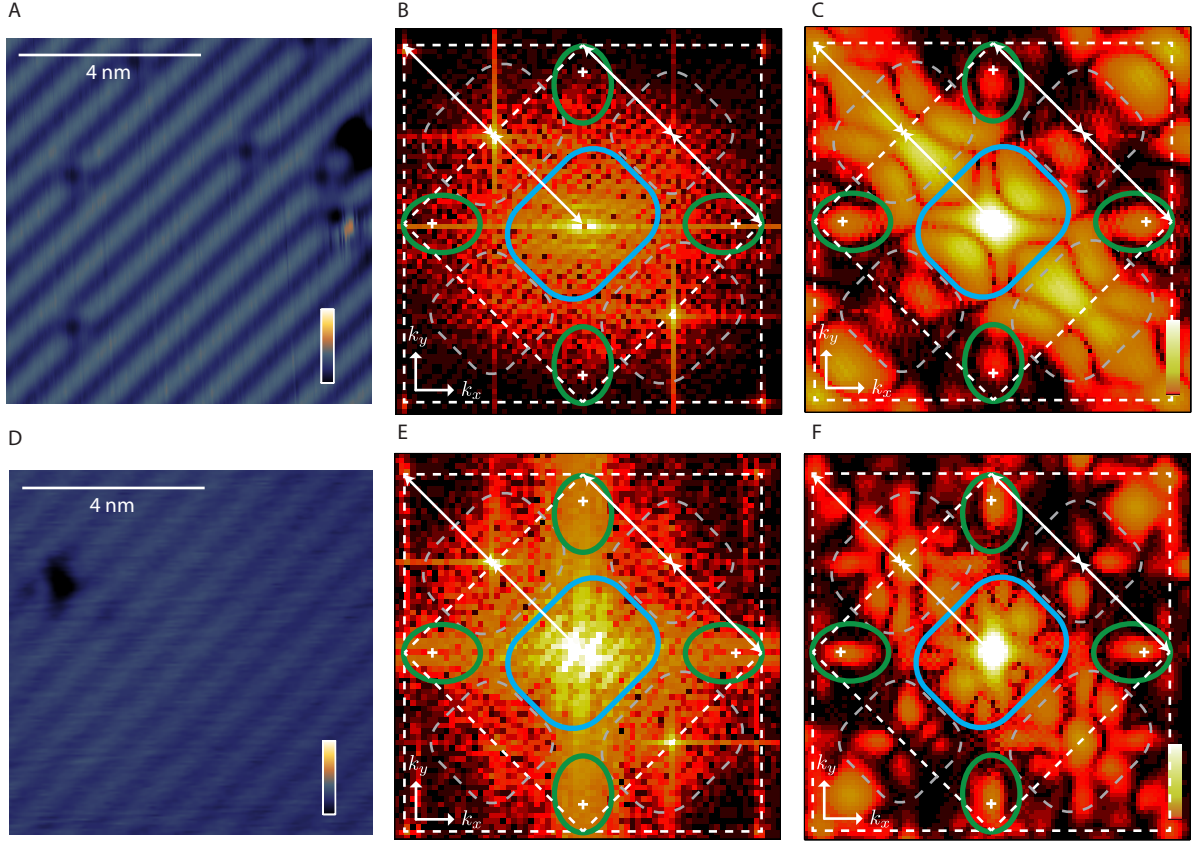


FIG. 8. A. Closeup $8 \text{ nm} \times 8 \text{ nm}$ of topography centered over donor 1 from the main text. Scale bars are (0,100 pm). B. Fourier transform of topography $z(x, y)$ in $20 \text{ nm} \times 20 \text{ nm}$ frame for donor 1, and overlay reciprocal space map from main text. Corners of the outer rectangle are reciprocal lattice vectors $2\pi/a_0(p, q)$ where $p = \pm 1$ and $q = \pm 1$. C. Fourier transform of donor 1 ground state from main text. D. Closeup $8 \text{ nm} \times 8 \text{ nm}$ of topography over donor 2 from the main text. Scale bars are (0,100 pm). E. Fourier transform of topography $z(x, y)$ in $20 \times 20 \text{ nm}$ frame for donor 2, and overlay reciprocal space map from main text. F. Fourier transform of donor 2 ground state from main text.

comfortably image single states with a spatial resolution of 1024×1024 pixels (for donor 1) and 512×512 pixels (for donor 2), in less than 30 minutes. The corresponding maximum spatial frequencies represented in the $L \times L = 20 \text{ nm} \times 20 \text{ nm}$ frames, providing the desired resolution $2\pi/L \approx (1/50)2\pi/a_0$, are $\sim 12(2\pi/a_0)$ (donor 1) and $\sim 6(2\pi/a_0)$ (donor 2).

Ellipsoid Fourier feature in real space

The expression for the real-space representation of the ellipsoid valley interference pattern in the main text was derived from the six-valley donor envelope function representation introduced by Kohn and Luttinger[25],

$$\Psi^i(\mathbf{r}) = \sum_{\mu} \alpha_{\mu}^i F_{\mu}(\mathbf{r}) \phi_{\mathbf{k}_{\mu}}(\mathbf{r}), \quad (4)$$

where $\mu = 1 \dots 6$ denotes the six conduction band minima in silicon, α_{μ}^i denotes the valley quantum number

describing the coherent valley population of the minimum, $F_{\mu}(\mathbf{r})$ is the envelope function, $\phi_{\mathbf{k}_{\mu}}(\mathbf{r}) = \exp(i\mathbf{k}_{\mu} \cdot \mathbf{r})u_{\mathbf{k}_{\mu}}(\mathbf{r})$ is the Bloch function for the band minimum, and $u_{\mathbf{k}_{\mu}}(\mathbf{r}) = \sum_{\mathbf{G}} A_{\mathbf{k},\mathbf{G}} \exp(i\mathbf{G} \cdot \mathbf{r})$ is a lattice periodic function over the reciprocal lattice vectors \mathbf{G} of the silicon crystal.

Supported by atomistic calculations, the measured subsurface donor ground states was found to have a bulk-like orbital structure and valley configuration. Consequently, we take $\alpha^1 = 1/\sqrt{6}(1, 1, 1, 1, 1, 1)$. As discussed in the main text, the ellipsoid features arise from products z and x (or y) valleys in $|\Psi(\mathbf{r})|^2$. Collecting the associated terms and assuming the ion position is located at $x = y = z = 0$, it is easy to show that their contribution to the probability density evaluated at $\mathbf{r} = (x, y, z_0)$ is given by

$$P(\mathbf{r}) = CF_z(\mathbf{r}) \times [F_x(\mathbf{r}) \cos(k_{\mu}x) + F_y(\mathbf{r}) \cos(k_{\mu}y)] \quad (5)$$

where $C = 8 \cos(k_{\mu}z_0) \sum_{\mathbf{G}} |A_{\mathbf{k}_{\mu},\mathbf{G}}|^2$. This expression has a global maximum at $x = y = 0$ when $\cos(k_{\mu}z_0) > 0$ and

a global minimum in the same location when $\cos(k_\mu z_0) < 0$. The ion position indicated in Figure 4 in the main text can be determined to high accuracy $\delta_x, \delta_y \ll 0.85(2\pi/a_0)$ by examining the global minimum in the real-space representation of the valley oscillation.

Atomistic theory

Atomistic predictions of the electron wavefunctions $\Psi_i(\mathbf{r})$ and probability densities $|\Psi_i(\mathbf{r})|^2$ of donor-bound states were obtained by empirical $\text{sp}^3\text{d}^5\text{s}^*$ tight-binding. Both were evaluated in the evanescent (vacuum) tail of the wavefunction $\Psi_1(\mathbf{r}) = \sum_{j,k} c_{j,k}^1 \varphi_j(\mathbf{r} - \mathbf{R}_k)$, where $c_{j,k}^1$ is the tight-binding representation of the ground state wavefunction, $\varphi_j(\mathbf{r})$ are s, p, and d Slater-type orbitals for silicon[40], and \mathbf{R}_k are positions of silicon atoms in the crystal. Evanescent (vacuum) tails of $\Psi(\mathbf{r})$ and $|\Psi(\mathbf{r})|^2$ were evaluated for a tip orbital position $\delta z = 0.45$ nm above the last atomic plane, assuming an s-wave tip[34].

Coefficients $c_{j,k}^1$ above were obtained by diagonalization of the tight binding Hamiltonian of ~ 1.4 million silicon atoms. A single arsenic atom was modeled as a Coulomb potential with on-site orbital energy corrections[6] successfully reproducing the measured donor energy spectrum including the valley-orbit splitting[41]. The influence of displacement of surface atoms associated with the 2×1 surface reconstruction on the tight binding Hamiltonian was computed by a generalization of Harrison's scaling law[42], assuming symmetric dimerization atomic displacements calculated elsewhere[43]. These models have been combined with the valence force field Keating model to describe atomistic strain relaxation in multi-million atom quantum dots in excellent agreement with experiments[44].

The full tight-binding Hamiltonian of silicon, the arsenic donor, and the hydrogen passivated surface was solved by a parallel Lanczos eigensolver to obtain the lowest energy donor eigenstates. The computations are performed using the atomistic tight-binding tool NEMO-3D utilizing nanohub.org resources, and requires about 5 hours on 40 processors to obtain 10 wavefunctions. A detailed description of this full-band non-perturbative method can be found in Refs 21 and 44.

Calculated single-electron excited states

Further details of tight-binding calculations of subsurface donor states are presented in this section. Two-dimensional Fourier transforms of wavefunctions $\Psi(x, y, z_0)$ and probability densities $|\Psi(x, y, z_0)|^2$ of the first six single-electron (D^0) eigenstates of a subsurface donor, calculated by tight binding, are given in Figure 9. The binding energy relative to the bottom of the bulk silicon conduction band is given, along with the dominant

valley contribution and the corresponding valley quantum numbers.

In particular, the predicted binding energy of the subsurface arsenic donor (51.5 meV) is only slightly smaller than that of the bulk arsenic donor (53.4 meV). Similarly, the valley-orbit splitting of the subsurface donor is 19.8 meV compared to the 21.1 meV splitting predicted for the bulk donor. The first excited state is α^4 -like and the second is α^5 -like. The third and fourth states are degenerate and are both linear combinations of α^2 and α^3 -like states, while the highest energy state in the manifold is α^6 -like. Recall for a donor in bulk silicon, the singlet has $\alpha^1 = 6^{-1/2}[1, 1, 1, 1, 1, 1]$, the triplet has $\alpha^2 = 2^{-1/2}[1, -1, 0, 0, 0, 0]$, $\alpha^3 = 2^{-1/2}[0, 0, 1, -1, 0, 0]$, and $\alpha^4 = 2^{-1/2}[0, 0, 0, 0, 1, -1]$, and the doublet has $\alpha^5 = 12^{-1/2}[-1, -1, -1, -1, 2, 2]$ and $\alpha^6 = 2^{-1}[1, 1, -1, -1, 0, 0]$.

Valley population

The absolute valley population for donor 1 was estimated by comparing the ratio of peaks at $\mathbf{k} = 0$ and $\mathbf{k} = 0.15(2\pi/a_0)(\pm 1, \pm 1)$ in measurements to calculations. In the main text we found that the ratio matched calculations for donor depths in zero field between $6.25a_0$ and $7.25a_0$. The corresponding absolute coherent valley population of the measured donor-bound state was estimated from the absolute coherent valley population calculated for depths $6.25a_0$ and $7.25a_0$. The latter was determined by a three-dimensional Fourier decomposition of the tight-binding wavefunction $\Psi(\mathbf{r}) = \sum_{i,j} c_{ij} \phi_i(\mathbf{r} - \mathbf{R}_j)$. Writing $\phi(r) = \sum_k \phi_i(\mathbf{k}) \exp(\mathbf{k} \cdot \mathbf{r})$ and $c_{ij} = c_i(\mathbf{R}_j)$ we obtain

$$\Psi(\mathbf{r}) = \sum_k e^{i\mathbf{k} \cdot \mathbf{r}} \left[\sum_i \phi_i(\mathbf{k}) \sum_j c_i(\mathbf{R}_j) e^{-i\mathbf{k} \cdot \mathbf{R}_j} \right]. \quad (6)$$

The term in block parenthesis is readily recognized as the Fourier component $\Psi(\mathbf{k})$ while the sum over j is a discrete Fourier transform, which was evaluated on a grid. The relative contribution of x , y and z valleys were obtained by integrating the three-dimensional distribution of valleys in $\Psi(\mathbf{k})$ obtained by this method. Results for x , y , and z valleys are shown in Figure 10A and 10B as a function of donor depth and peak ratio.

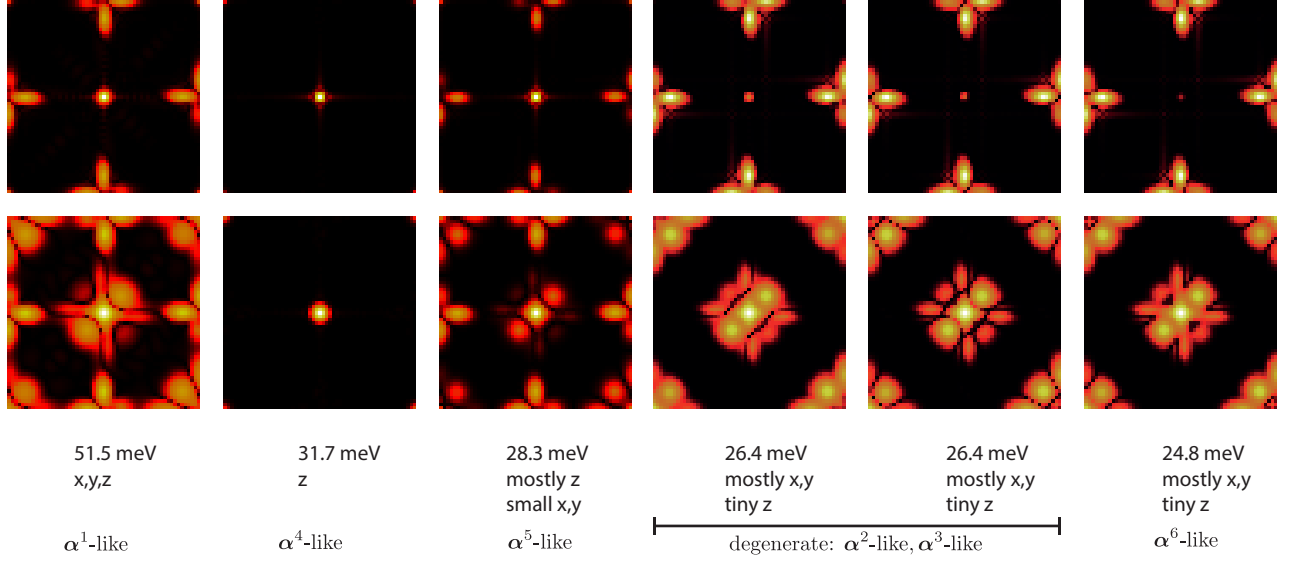


FIG. 9. Fourier transform of tight-binding calculations for subsurface donor $6.25a_0 \approx 2.8$ nm below hydrogen-terminated silicon surface, for region $k_x = [-2\pi/a_0, 2\pi/a_0]$ and $k_y = [-2\pi/a_0, 2\pi/a_0]$. First row is $\Psi(\mathbf{r})$. Second row is $|\Psi(\mathbf{r})|^2$. Columns $i = 1 \dots 6$ are first 6 valley eigenstates. Energies, and dominant contribution to valley configuration are listed in each column. Corresponding bulk-like valley configuration is given.

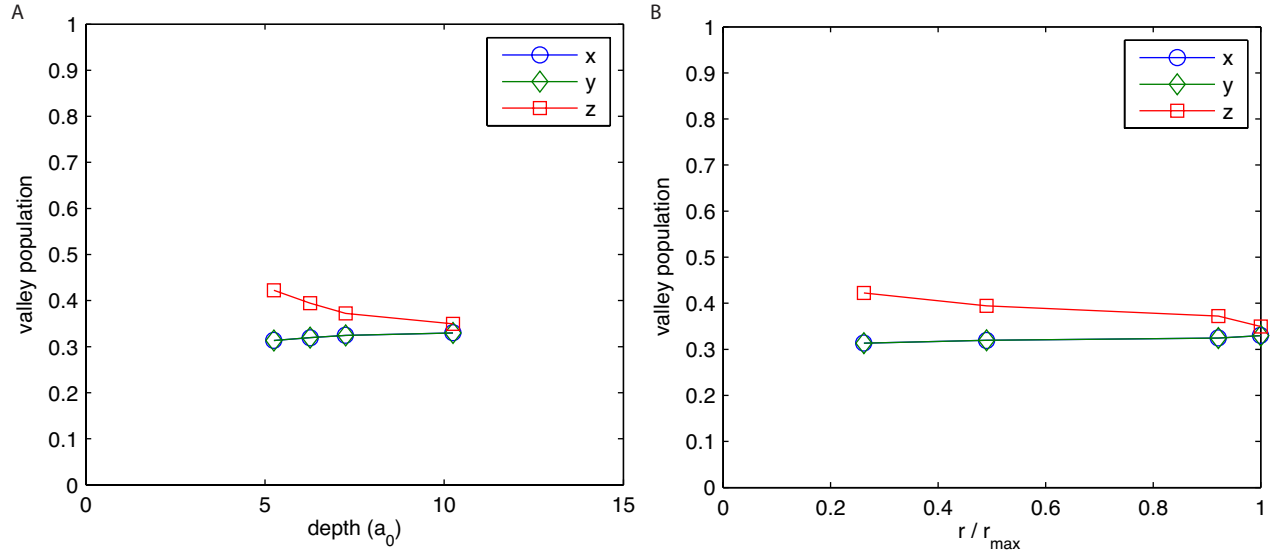


FIG. 10. Relative distribution of probability amplitudes of donor wavefunction between x , y , and z valleys as a function of (A) donor depth, and as a function of (B) peak ratio.

* s.rogge@unsw.edu.au

- [1] A. M. Tyryshkin, S. Tojo, J. J. L. Morton, H. Riemann, N. V. Abrosimov, P. Becker, H.-J. Pohl, T. Schenkel, M. L. W. Thewalt, K. M. Itoh, and S. A. Lyon, *Nature Materials* **11**, 143 (2011).
- [2] M. Steger, K. Saeedi, M. L. W. Thewalt, J. J. L. Morton, H. Riemann, N. V. Abrosimov, P. Becker, and H. J. Pohl, *Science* **336**, 1280 (2012).
- [3] B. E. Kane, *Nature* **393**, 133 (1998).
- [4] J. J. L. Morton, D. R. McCamey, M. A. Eriksson, and S. A. Lyon, *Nature* **479**, 345 (2011).
- [5] S. Goswami, K. A. Slinker, M. Friesen, L. M. McGuire, J. L. Truitt, C. Tahan, L. J. Klein, J. O. Chu, P. M. Mooney, D. W. van der Weide, R. Joynt, S. N. Coppersmith, and M. A. Eriksson, *Nature Physics* **3**, 41 (2006).
- [6] G. P. Lansbergen, R. Rahman, C. J. Wellard, I. Woo, J. Caro, N. Collaert, S. Biesemans, G. Klimeck, L. C. L. Hollenberg, and S. Rogge, *Nature Physics* **4**, 656 (2008).
- [7] B. Roche, E. Dupont-Ferrier, B. Voisin, M. Cobian, X. Jehl, R. Wacquez, M. Vinet, Y. M. Niquet, and M. Sanquer, *Phys. Rev. Lett.* **108**, 206812 (2012).
- [8] C. H. Yang, A. Rossi, R. Ruskov, N. S. Lai, F. A. Mohiyaddin, S. Lee, C. Tahan, G. Klimeck, A. Morello, and A. S. Dzurak, *Nat Comms* **4** (2013).
- [9] B. Koiller, X. Hu, and S. Das Sarma, *Phys. Rev. Lett.* **88** (2001).
- [10] C. Wellard and L. Hollenberg, *Phys. Rev. B* **72**, 085202 (2005).
- [11] A. Rycerz, J. Tworzydło, and C. W. J. Beenakker, *Nature Physics* **3**, 172 (2007).
- [12] Ö. Soykal, R. Ruskov, and C. Tahan, *Phys. Rev. Lett.* **107**, 235502 (2011).
- [13] D. Culcer, A. Saraiva, B. Koiller, X. Hu, and S. Das Sarma, *Phys. Rev. Lett.* **108** (2012).
- [14] F. Pei, E. A. Laird, G. A. Steele, and L. P. Kouwenhoven, *Nature Nanotech* **7**, 630 (2012).
- [15] J. Isberg, M. Gabrysch, J. Hammersberg, S. Majdi, K. K. Kovi, and D. J. Twitchen, *Nature Materials* **12**, 760 (2013).
- [16] N. Tombros, A. Veligura, J. Junesch, M. H. D. Guimarães, I. J. Vera-Marun, H. T. Jonkman, and B. J. van Wees, *Nature Physics* **7**, 697 (2011).
- [17] M. Fuechle, J. A. Miwa, S. Mahapatra, H. Ryu, S. Lee, O. Warschkow, L. C. L. Hollenberg, G. Klimeck, and M. Y. Simmons, *Nature Nanotech* **7**, 242 (2012).
- [18] J. J. Pla, K. Y. Tan, J. P. Dehollain, W. H. Lim, J. J. L. Morton, D. N. Jamieson, A. S. Dzurak, and A. Morello, *Nature* **489**, 541 (2012).
- [19] J. J. Pla, K. Y. Tan, J. P. Dehollain, W. H. Lim, J. J. L. Morton, F. A. Zwanenburg, D. N. Jamieson, A. S. Dzurak, and A. Morello, *Nature* **496**, 334 (2013).
- [20] M. Calderón, B. Koiller, X. Hu, and S. Das Sarma, *Phys. Rev. Lett.* **96** (2006).
- [21] R. Rahman, C. Wellard, F. Bradbury, M. Prada, J. Cole, G. Klimeck, and L. Hollenberg, *Phys. Rev. Lett.* **99**, 036403 (2007).
- [22] B. Trauzettel, D. V. Bulaev, D. Loss, and G. Burkard, *Nature Physics* **3**, 192 (2007).
- [23] A. Saraiva, M. Calderón, X. Hu, S. Das Sarma, and B. Koiller, *Phys. Rev. B* **80**, 081305 (2009).
- [24] F. A. Zwanenburg, A. S. Dzurak, A. Morello, M. Y. Simmons, L. C. L. Hollenberg, G. Klimeck, S. Rogge, S. N. Coppersmith, and M. A. Eriksson, *Rev. Mod. Phys.* **85**, 961 (2013).
- [25] W. Kohn and J. Luttinger, *Phys. Rev.* **98**, 915 (1955).
- [26] S. Pantelides and C. Sah, *Phys. Rev. B* **10**, 621 (1974).
- [27] P. Van Mieghem, *Rev. Mod. Phys.* **64**, 755 (1992).
- [28] J. L. Pitters, P. G. Piva, and R. A. Wolkow, *Journal of Vacuum Science & Technology B: Microelectronics and Nanometer Structures* **30**, 021806 (2012).
- [29] F. Marczinowski, J. Wiebe, J. M. Tang, M. Flatté, F. Meier, M. Morgenstern, and R. Wiesendanger, *Phys. Rev. Lett.* **99**, 157202 (2007).
- [30] P. M. Koenraad and M. E. Flatté, *Nature Materials* **10**, 91 (2011).
- [31] E. Foxman, P. McEuen, U. Meirav, N. Wingreen, Y. Meir, P. Belk, N. Belk, M. Kastner, and S. Wind, *Phys. Rev. B* **47**, 10020 (1993).
- [32] Mol, J A, J. Salfi, J. A. Miwa, M. Y. Simmons, and S. Rogge, *Phys. Rev. B* **87**, 245417 (2013).
- [33] K. Sinthiptharakoon, S. R. Schofield, P. Studer, V. Brázdová, C. F. Hirjibehedin, D. R. Bowler, and N. J. Curson, *arxiv*, 1307.6890 (2013).
- [34] C. J. Chen, *Phys. Rev. B* **42**, 8841 (1990).
- [35] J. Chelikowsky and M. Cohen, *Phys. Rev. B* **10**, 5095 (1974).
- [36] M. Cohen and T. Bergstresser, *Phys. Rev.* **141**, 789 (1966).
- [37] H. Hasegawa, *Phys. Rev.* **118**, 1523 (1960).
- [38] A. Morello, J. J. Pla, F. A. Zwanenburg, K. W. Chan, K. Y. Tan, H. Huebl, M. Möttönen, C. D. Nugroho, C. Yang, J. A. van Donkelaar, A. D. C. Alves, D. N. Jamieson, C. C. Escott, L. C. L. Hollenberg, R. G. Clark, and A. S. Dzurak, *Nature* **467**, 687 (2010).
- [39] R. Rahman, S. H. Park, T. B. Boykin, G. Klimeck, S. Rogge, and L. C. L. Hollenberg, *Phys. Rev. B* **80** (2009).
- [40] E. Nielsen, R. Rahman, and R. P. Muller, *Journal of Applied Physics* **112**, 114304 (2012).
- [41] A. K. Ramdas and S. Rodriguez, *Reports on Progress in Physics* **44**, 1297 (1981).
- [42] T. Boykin, G. Klimeck, R. Bowen, and F. Oyafuso, *Phys. Rev. B* **66**, 125207 (2002).
- [43] B. I. Craig and P. V. Smith, *Surface Science* **226**, L55 (1990).
- [44] G. Klimeck, S. S. Ahmed, H. Bae, N. Kharche, S. Clark, B. Haley, S. Lee, M. Naumov, H. Ryu, F. Saied, M. Prada, M. Korkusinski, T. B. Boykin, and R. Rahman, *IEEE Trans. Electron Devices* **54**, 2079 (2007).